The Fundamentals of Transport in Living Tissues Quantified by Medical Imaging Technologies

2

Sebastian Hirsch, Tobias Schaeffter, and Ingolf Sack

Abstract

Physiology is the science of the mechanical, physical, bioelectrical, and biochemical functions of living systems. All physiological processes are based on physical and biochemical principles. Quantitative medical imaging exploits these principles to measure parameters of those processes noninvasively in vivo. Parameters measured by quantitative medical imaging have to be in agreement with values that would be obtained from standardized measurements from physics or material sciences, if these were applicable for living tissues. Technical advancements have led to the emergence of various methods for quantifying biophysical and constitutive tissue parameters. This chapter focuses on quantitative medical imaging of physiological processes that are related to different types of physical transport mechanisms. More specifically, we will show that continuity of mass and energy can be interpreted as overarching principles that govern seemingly unrelated modes of energy or mass transport. For this, the derived transport equations will be reviewed from the perspective of medical imaging modalities such as magnetic resonance imaging (MRI), positron emission tomography (PET), or ultrasound with a focus on water diffusion, blood perfusion, fluid flow, and mechanical wave propagation.

S. Hirsch
Department of Medical Informatics, Charité – Universitätsmedizin Berlin, Berlin, Germany

T. Schaeffter
Medical Physics and Metrological Information Technology Physikalisch-Technische Bundesanstalt, Berlin, Germany

I. Sack (✉)
Department of Radiology, Charité – Universitätsmedizin Berlin, Berlin, Germany
e-mail: ingolf.sack@charite.de

Notation

Attention is paid to keep the mathematical notation as consistent and self-explanatory as possible. The following conventions were used:

- Matrices, tensors, and vectors are denoted by bold, upright Latin or Greek letters: $\mathbf{a} = \mathbf{C} \cdot \mathbf{b}$.
- The dot operator "·" is used exclusively to denote the scalar product of two vectors or tensorial expressions leading always to a reduction: $a = \mathbf{b} \cdot \mathbf{c} \equiv \sum_i b_i c_i$.
- Matrix multiplication which preserves or increases the rank of a tensor is denoted by two adjacent tensorial symbols: $\mathbf{a} = \mathbf{bc}$.
- Where appropriate, temporal derivatives are marked by a dot and spatial derivatives by an apostrophe: $\dfrac{\partial f}{\partial t} = \dot{f}$ and $\dfrac{\partial f}{\partial r} = f'$.
- Summation over an index is always specified explicitly by the sum symbol.
- Only indices or exponents that take numerical values are printed in italics; super- or subscripts that serve as a specification are always printed upright: x_i, a^b, and u_{shear}.
- The complex unit is always represented by an upright letter to make it distinguishable from an index: $\sqrt{-1} = \mathrm{i} \leftrightarrow u_i, i \in \mathbb{N}$.
- Fourier transform is denoted either by FT or a diacritic symbol: $FT(\mathbf{u}) \equiv \tilde{\mathbf{u}}$.

List of Symbols

The following table lists commonly used mathematical symbols. Note that some symbols are reused in a local context to denote something else, but this will always be explained in the text.

Roman symbols	
$\mathbf{B}$, BF, b	Magnetic field, blood flow, b-value
$\mathbf{C}$, C, c	Elasticity tensor, particle concentration, wave speed
D	Diffusion constant
E	Energy
$\mathbf{G}$, g, G^*	Linear magnetic field gradient, gradient amplitude, complex shear modulus
i, (i)	Imaginary unit, index of incident wave
K	Compression modulus
$\mathbf{m}$, m	Magnetic moment, mass
N	Gaussian distribution function
$\mathbf{P}$	Flux vector
R, (r), $\mathbf{r}$, r	Reflection coefficient, index of reflected wave, position vector, traveled distance
S	MRI signal
T, t, (t)	Transmission coefficient, time, index of transmitted waves

u	Particle deflection
v	Deflection velocity
x, y, z	Spatial coordinates
Greek symbols	
α	Springpot interpolation parameter
δ	Dirac delta distribution, loss angle
$\boldsymbol{\varepsilon}$	Strain tensor
η	Viscosity
φ	Spin phase
γ	Gyromagnetic ratio
κ	Lumped springpot modulus
λ	Perfusion partition coefficient
μ	Shear modulus
Θ	Heaviside function
ρ	Mass density
$\boldsymbol{\sigma}$	Stress tensor
ς	Compression viscosity
$\tau, (\tau_{\Delta})$	Time delay, application time of MRI gradient (delay between MRI gradients)
ω	Angular frequency
Mathematical operators	
$\nabla, \nabla\times, \nabla\cdot$	Gradient operator (vector), curl, divergence
Δ	Laplacian operator
FT	Fourier transform
1	Identity operator

2.1   Introduction

This chapter pursues two objectives. Firstly, transport phenomena in the human body will be discussed from a physics point of view. Secondly, we will explain how medical imaging—especially magnetic resonance imaging (MRI)—can be used to assess and quantify these transport phenomena.

For the physics part, we follow a route that is different from most textbook discussions of waves, diffusion, and flow, which are based on Newton's law. Instead, we will show that the continuity equation and the associated concept of conservation of mass and energy can be understood as the overarching principles applying to all these transport mechanisms.

Physiology is the science of the mechanical, physical, bioelectrical, and biochemical functions of living systems. Physiology is closely related to anatomy, the study of form, and both are studied in tandem as part of a medical curriculum. Biomedical imaging allows noninvasive assessment of anatomy and physiology, i.e., form and function. Physiology can be assessed in more detail by quantitative imaging techniques when the underlying physical principles are known. In particular, the transport of particles, mass, or energy is fundamental to many living

processes. In fact, all vital functions depend on the transport of blood, oxygen, nutrients, metabolites, or electrical signals. All transport mechanisms have in common that they involve a *local density* (or concentration) of a substance (such as nutrients) or energy and *flux*, which describes the motion of the said quantity. The fundamental relationship between density and flux is defined by the continuity equation [1]:

$$\frac{\partial \rho}{\partial t} = -\nabla \cdot \mathbf{P}, \tag{2.1}$$

which states that any influx ($\mathbf{P}$) of energy or mass into a volume has to be balanced by a change in energy or mass density (ρ) within that volume. $\nabla \cdot \mathbf{P}$ denotes the divergence of the flux, which quantifies the local source or sink density of the flux field. ∇ is a vector operator whose components are first-order spatial derivative operators. Equation (2.1) means that mass or energy can neither be created nor destroyed. Furthermore, the continuity equation states that matter is conserved *locally*. This is a strong conservation statement and the foundation of many quantitative imaging techniques, which account for mass and energy within a given volume. $\mathbf{P}$ is the flux vector whose components describe the flow of mass or energy with velocity $\mathbf{v}$ through a surface element of unit area perpendicular to $\mathbf{v}$:

$$\mathbf{P} = \rho \, \mathbf{v}. \tag{2.2}$$

Equations (2.1) and (2.2) state that flow occurs along the negative density gradient, meaning that flow is induced from sources ($\nabla \cdot \mathbf{P} > 0$) to sinks ($\nabla \cdot \mathbf{P} < 0$). Furthermore, according to Eq. (2.1), wherever the divergence of flux ($\nabla \cdot \mathbf{P}$) is distinct from zero, mass or energy density has to change.

Transport phenomena quantified by medical imaging technologies include many scales and various physical principles. Based on the continuity equation (2.1), we will derive the governing (equilibrium) equations and measured quantities for the following transport mechanisms:

- Diffusion
- Energy transport by mechanical waves
- Fluid flow
- Perfusion

The complexity of biological structures naturally leads to overlapping physical representations of these mechanisms. This motivates our intention to review the underlying principles from the perspective of medical imaging, which, however, often means that we must make assumptions and introduce simplifications in order to treat the basic equations in a straightforward manner. The following sections therefore briefly compile the basic equations starting with Eq. (2.1) to facilitate the comparison of the physical concepts of quantitative medical imaging with a focus on mass and energy transport.

2.2   Diffusion

Diffusion is ubiquitous in nature and related to any type of stochastic motion of molecules and particles driven by Brownian motion. Diffusion is temperature dependent, since the average kinetic energy per particle increases with temperature, so that particles can travel farther within a given time span when the temperature is higher [2, 3].

   In tissues, many vital transport mechanisms are governed by diffusion; and detecting changes in diffusion can indicate diseases with high sensitivity (see Chap. 17). Therefore, measurement of diffusion of water or tracers by medical imaging modalities has been part of clinical routine for a long time. In our generalized treatment of transport physics, we derive the equilibrium equation for diffusion from the continuity equation using Fick's first law. Fick's law states that, in equilibrium, the steady-state flux of particles occurs along the negative density gradient (or concentration gradient), i.e., from high to low densities, and with a velocity that is proportional to the density gradient:

$$\mathbf{P} = -D\nabla\rho. \tag{2.3}$$

   D is called the *diffusion coefficient* and is expressed in the unit of area per unit time, typically mm^2/s in diffusion-weighted MRI. D quantifies how easily a particle can move in the direction of flux vector $\mathbf{P}$ according to Fick's law. Combining Eqs. (2.1) and (2.3) yields

$$\frac{\partial\rho}{\partial t} = D\Delta\rho, \tag{2.4}$$

which constitutes the diffusion equation in three dimensions. Δ is the 3D Laplace operator as obtained by the product of gradient vectors: $\Delta = \nabla\cdot\nabla = \dfrac{\partial^2}{\partial x^2} + \dfrac{\partial^2}{\partial y^2} + \dfrac{\partial^2}{\partial z^2}$.

The 3D diffusion equation is satisfied by a normal Gaussian distribution of probability N of the particles having traveled a distance r [4]:

$$\rho(r,t) \propto N(r,t) = \frac{1}{(4\pi Dt)^{\frac{3}{2}}}\, \mathrm{e}^{-\frac{r^2}{4Dt}}. \tag{2.5}$$

   This Gaussian distribution has standard deviation $\sqrt{2Dt}$ and variance $2Dt = \langle\mathbf{r}^2\rangle$. The relationship $t \propto \langle\mathbf{r}^2\rangle$ applies to *regular diffusion*. Equation (2.5) highlights the probabilistic nature of diffusion: at any time t, particle density ρ is distributed over a continuum of radii r. This means that particle velocities and thus kinetic energies are within the whole range of values from zero to infinity (in a nonrelativistic model for the relationship between speed and kinetic energy). Consequently, already at the beginning of the diffusion process, the probability of finding diffusing particles at arbitrarily large distances is larger than zero. As the diffusion process continues, the particle cloud spreads out, and the probability of finding particles at large

distances increases, while the concentration at the source decreases. This process is thermodynamically driven by an increase in entropy due to the increasing disorder in the system. Thus, passive diffusion is a spontaneous process and does not require input of energy. Section 7.3 explains how diffusion can be measured by MRI along with classifications of nonregular diffusion processes as detected by MRI in biological tissues.

It is important to note that the term "density" or "concentration," as used in the context of Eqs. (2.3)–(2.5), does not have to be an actual mass density but can rather refer to the "density of specifically labeled particles." The meaning of this statement becomes clearer when analyzing diffusion in a glass of pure water. Ignoring gravitational effects, the density of water is equal everywhere, so that the density gradient in Eq. (2.3) vanishes and thus the flux becomes zero. However, this is not physically correct. The underlying process is called "self-diffusion." It can be understood by assuming that the water molecules in each small volume element are assigned a specific label and that the label is unique for each volume element. In that case, "density" refers to the concentration of water molecules carrying one specific label. All volume elements act as the sources of many separate diffusion processes running in parallel. Initially, all molecules with a specific label are contained in the same volume element. As time passes, through random motion, molecules leave their original volume element and diffuse into other volume elements. Thus, the concentration of molecules with a specific label broadens over time, with the concentration being represented by a Gaussian function as described above (Fig. 2.1). In the long-time limit, all volume elements contain water molecules from all other volume elements, i.e., a uniform mixture of labels. However, since the whole process consists of water molecules moving around, the bulk density remains constant. In the context of diffusion MRI, the labeling of water molecules is achieved by imposing a position-dependent spin phase onto every spin ensemble, as shall be described in Sect. 2.7.3.
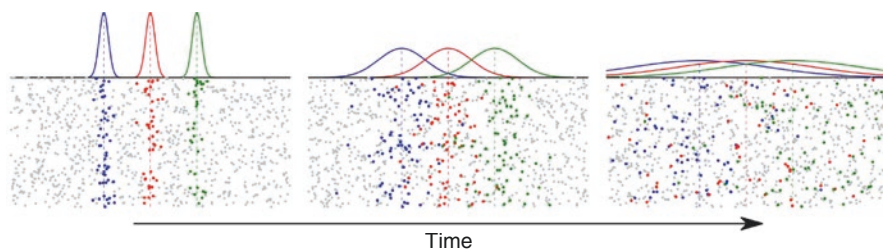

Fig. 2.1 Illustration of one-dimensional self-diffusion. Each dot represents a particle (e.g., a water molecule). Initially, particles in three volume elements are labeled, indicated red, green, and blue. Over time, the particles diffuse along the horizontal axis, as can be seen from the broadening of the corresponding probability distributions. Nevertheless, the bulk density remains unchanged, since unlabeled particles compensate the motion of the labeled particles. The dashed lines indicate the positions of the original labeling

2.3   Wave Transport

A number of imaging modalities including ultrasound, elastography, and photo-acoustic tomography exploit the propagation of classical waves for generating image contrast. Mechanical waves can be understood as the propagation of a distortion of the mechanical equilibrium state through time and space [2]. Wave propagation is associated with transport of energy by local particle deflections, i.e., by local mass displacements around equilibrium position in a static reference coordinate system (see Fig. 2.2). The deformation of an object can be described in terms of the
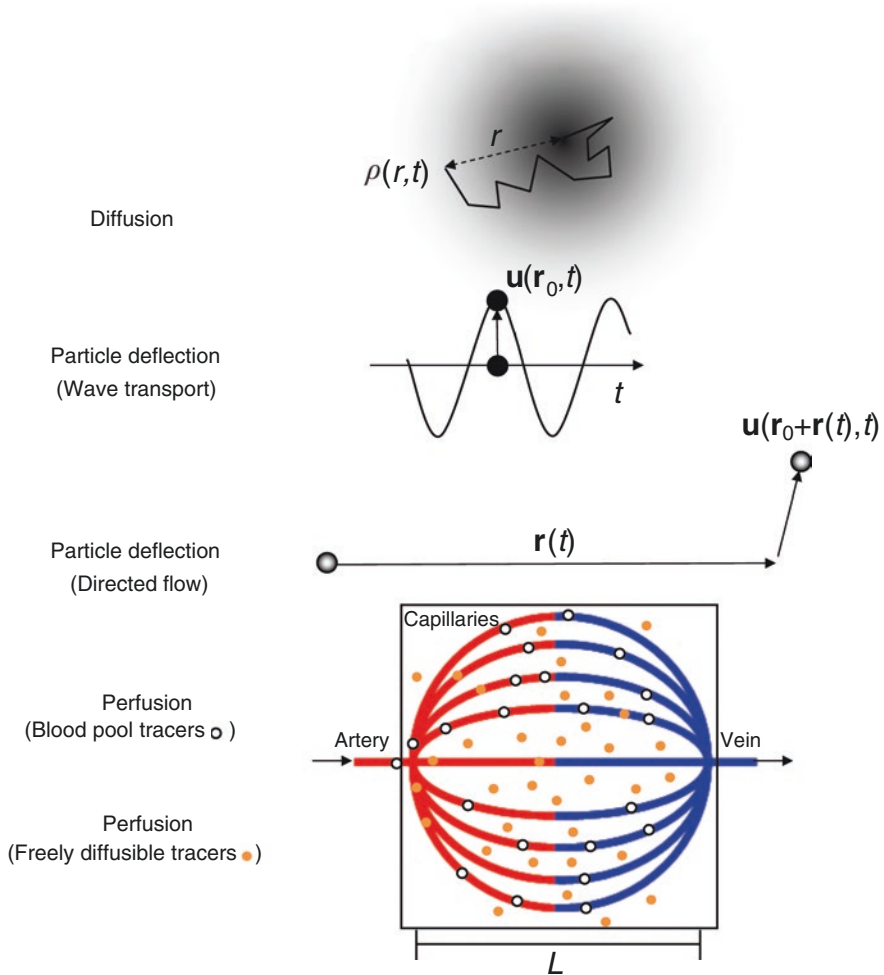

Fig. 2.2 Notation of transport phenomena addressed in this chapter

displacement field **u** in the sense that every point **r** is shifted to a different position **r** + **u**(**r**, *t*). This displacement field **u** is the dynamic parameter behind ultrasound-based medical imaging or elastography. Before we begin the discussion of mechanical wave propagation and how it is related to the continuity equation, we will first introduce elementary terminology, namely, *stress* and *strain*. More details can be found in standard textbooks of elasticity theory and continuum mechanics such as [5] and [6].

2.3.1   Strain, Stress, and Linear Elasticity Coefficients

Strain describes the elastic deformation a body has undergone upon exertion of a force [6]. Strain is usually measured as displacement **u** relative to the size *Δ***r** of the deformed body. A compact tensor notation of **u** over *Δ***r** is given by the infinitesimal linear strain tensor **ε** with components

$$\varepsilon_{ij} = \frac{1}{2}\left(\frac{\partial u_i}{\partial r_j} + \frac{\partial u_j}{\partial r_i}\right) = \frac{1}{2}\left(\nabla\mathbf{u} + \left(\nabla\mathbf{u}\right)^T\right). \tag{2.6}$$

$\nabla\mathbf{u}$ is the Jacobian of the displacement field, i.e., the matrix that includes all spatial derivatives, $\left(\nabla\mathbf{u}\right)_{ij} = \dfrac{\partial u_i}{\partial r_j}$. **ε** is a symmetric (i.e., $\varepsilon_{ij} = \varepsilon_{ji}$) tensor of rank 2 which can be expressed as a 3×3 matrix. Due to its symmetry, only six of its nine entries are independent. Any strain in a material is caused by a force **F** acting on a surface element A_j. $j \in \{1, 2, 3\}$ denotes the direction of surface normal vectors along the Cartesian coordinates (see Fig. 2.3). Force per area defines stress, i.e.,
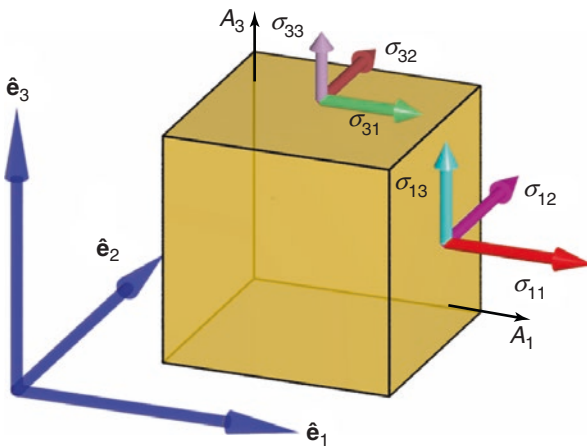

Fig. 2.3 Notation of the stress tensor elements which are defined by the directions of acting forces and surface normals A_j

$$\sigma_{ij} = \frac{F_i}{A_j}, \tag{2.7}$$

which is a tensor of rank 2, analogous to strain. The diagonal components of the stress tensor $\boldsymbol{\sigma}$, σ_{ii}, act orthogonally on the three surfaces A_i. The sum $\sum_i \sigma_{ii}$ is proportional to the negative pressure acting against volumetric changes, i.e., compression or dilatation. The off-diagonal entries σ_{ij}, $i \neq j$, characterize stresses tangential to their respective surfaces. Tangential stresses exert a torque on the volume element, causing shear deformation while preserving volume. If the resultant torque of all stresses does not vanish, the cube will rotate. Therefore, the necessary and sufficient condition for a static (equilibrium) configuration is that all tangential (shear) stress components cancel each other, which is fulfilled if $\sigma_{ij} = \sigma_{ji}$. Thus, the stress tensor possesses the same symmetry as the strain tensor.

The relationship between stress and strain is, in linear approximation, characterized by a constant rank-four tensor $\mathbf{C}$ which contains all the elastic coefficients necessary to describe the stress throughout a material that causes or is caused by a given strain:

$$\boldsymbol{\sigma} = \mathbf{C} \cdot \boldsymbol{\varepsilon} \; (\text{tensor notation}), \tag{2.8}$$

$$\sigma_{ij} = \sum_{k=1}^{3} \sum_{l=1}^{3} C_{ijkl} \varepsilon_{kl} \; (\text{component notation}). \tag{2.9}$$

This is Hooke's law—the most fundamental constitutive law in material science, which accounts for a spring-like elastic response of a solid in the limit of small deformations. Since $\mathbf{C}$ is a fourth-order tensor, it formally has $3^4 = 81$ elements, of which only 21 are independent because of symmetry in the case of the most general anisotropic solid. Applications of Hooke's law to biological materials usually require far fewer coefficients. In a transversely isotropic elastic material (featuring a single plane of isotropy and a principal axis orthogonal to that plane), $\mathbf{C}$ has only five independent coefficients, whereas under perfect isotropy, only two independent coefficients exist [6]. There are several ways to parameterize an isotropic material in terms of pairs of elastic moduli such as shear modulus μ and compression modulus K, Young's modulus E and Poisson's ratio ν or both Lamé coefficients (the second of which again being the shear modulus μ). All combinations are equivalent and can be converted to any other combination. As an example, Hooke's law of an isotropic material expressed in terms of compression modulus K and shear modulus μ is

$$\boldsymbol{\sigma} = \left(K - \frac{2}{3}\mu \right)(\nabla \cdot \mathbf{u})\mathbf{I} + \mu\boldsymbol{\varepsilon}, \tag{2.10}$$

where $\mathbf{I}$ is the 3×3 unit matrix and $(\nabla \cdot \mathbf{u})$ signifies volumetric strain. Due to the high water content, soft biological tissues normally have much higher compression moduli than shear moduli, since water has a very high compression modulus of approximately 2.2 GPa but can undergo shear deformation with no resistive response at all (see Table 12.1 in Chap. 12).

2.3.2 Mechanical Waves

The equilibrium equation of classical wave fields $\mathbf{u}$ is obtained from the continuity of dynamic strain energy. Hence, we need to account for kinetic energy density E_{kin} and potential energy density E_{pot} of the displacement field $\mathbf{u}$ in order to assess total energy density $E = E_{\text{kin}} + E_{\text{pot}}$. Similar to the kinetic energy of a mass point with velocity $\dot{u}$ ($E_{\text{kin}} = \dfrac{1}{2} m \dot{u}^2$), the kinetic energy density of a coherent wave field $\mathbf{u}$ can be expressed as

$$E_{\text{kin}} = \frac{1}{2} \rho \dot{\mathbf{u}} \cdot \dot{\mathbf{u}} = \rho \frac{1}{2} \sum_{i=1}^{3} \dot{u}_i^2. \tag{2.11}$$

To proceed with potential energy, we need the stress-strain relation that we introduced in the previous section.

2.3.2.1 From the Continuity of Dynamic Strain Energy to the Navier Equation

Hooke's law is directly linked to the internal strain energy (potential energy) density of an elastically deformed body by [5]

$$E_{\text{pot}} = \frac{1}{2} \boldsymbol{\sigma} \cdot \boldsymbol{\varepsilon} = \frac{1}{2} \sum_{i=1}^{3} \sum_{j=1}^{3} \sum_{k=1}^{3} \sum_{l=1}^{3} C_{ijkl} \varepsilon_{ij} \varepsilon_{kl}. \tag{2.12}$$

The total energy density, $E = E_{\text{kin}} + E_{\text{pot}}$, is the preserved quantity of interest for wave propagation. We therefore formulate the continuity equation (2.1) in terms of energy density:

$$\frac{\partial E}{\partial t} = \frac{\partial \left(E_{\text{kin}} + E_{\text{pot}} \right)}{\partial t} = -\nabla \cdot \mathbf{P}. \tag{2.13}$$

The left-hand side of Eq. (2.13) can be expanded by inserting E_{kin} from Eq. (2.11) and E_{pot} from Eq. (2.12):

$$\frac{\partial E}{\partial t} = \rho \underbrace{\frac{1}{2} \frac{\partial}{\partial t} \left(\frac{\partial \mathbf{u}}{\partial t} \cdot \frac{\partial \mathbf{u}}{\partial t} \right)}_{\rho \ddot{\mathbf{u}} \cdot \dot{\mathbf{u}}} + \underbrace{\frac{1}{2} \frac{\partial}{\partial t} (\mathbf{C} \cdot \boldsymbol{\varepsilon} \cdot \boldsymbol{\varepsilon})}_{\boldsymbol{\sigma} \cdot \dot{\boldsymbol{\varepsilon}}}. \tag{2.14}$$

The right-hand side of Eq. (2.13) denotes the flux of strain energy into a volume element. The flux of strain energy is stress multiplied by deflection velocity as given in [7]

$$\begin{aligned} \mathbf{P} &= -\boldsymbol{\sigma} \cdot \dot{\mathbf{u}} \\ \Rightarrow \nabla \cdot \mathbf{P} &= \left(\nabla \cdot \boldsymbol{\sigma} \right) \cdot \dot{\mathbf{u}} + \boldsymbol{\sigma} \cdot \nabla \dot{\mathbf{u}}. \end{aligned} \tag{2.15}$$

Combining Eq. (2.14) with Eq. (2.15) leads to

$$\rho \ddot{\mathbf{u}} \cdot \dot{\mathbf{u}} + \boldsymbol{\sigma} \cdot \dot{\boldsymbol{\varepsilon}} = (\nabla \cdot \boldsymbol{\sigma}) \cdot \dot{\mathbf{u}} + \boldsymbol{\sigma} \cdot \nabla \dot{\mathbf{u}}$$

$$\Rightarrow \rho \ddot{\mathbf{u}} \cdot \dot{\mathbf{u}} = (\nabla \cdot \boldsymbol{\sigma}) \cdot \dot{\mathbf{u}}.$$

(2.16)

In the above equation, we exploited the fact that $\boldsymbol{\sigma} \cdot (\nabla \dot{\mathbf{u}} - \dot{\boldsymbol{\varepsilon}}) = 0$ due to the tensorial symmetries of $\boldsymbol{\sigma}$ and $\boldsymbol{\varepsilon}$. Equation (2.16) agrees with Newton's second law, which can be expressed as

$$\rho \ddot{\mathbf{u}} = \nabla \cdot \boldsymbol{\sigma}$$

(2.17)

and which also constitutes the equilibrium equation for elastic waves. Equation (2.17) can be expanded for isotropic materials in terms of compression modulus K and shear modulus μ as defined in Eq. (2.10):

$$\rho \ddot{\mathbf{u}} = \left(K + \frac{4}{3} \mu \right) \nabla (\nabla \cdot \mathbf{u}) - \mu \nabla \times (\nabla \times \mathbf{u}).$$

(2.18)

In the literature, Eq. (2.18) is often referred to as Navier equation for isotropic, homogeneous solids. It has the characteristic form of a wave equation, relating a second-order temporal derivative with second-order spatial derivatives. For simplicity we neglected all spatial variations of coefficients K and μ, leading us to the assumption of zero spatial derivatives of the elastic coefficients. This *assumption of local homogeneity* is applied in many treatments of the wave equation in wave-inversion-based imaging modalities. Equation (2.18) illustrates that the full displacement field is a superposition of two separate fields: a compression field ($\nabla \cdot \mathbf{u}$) and a shear field ($\nabla \times \mathbf{u}$). Each term represents decoupled and independent types of motion, which can be separated into two independent wave equations by virtue of Helmholtz decomposition (see Chap. 4, Eqs. (4.8)–(4.10).) [5]. Applying the divergence operator or curl operator to Eq. (2.18) yields two separate equations for compression waves and shear waves, respectively:

$$\rho (\nabla \cdot \ddot{\mathbf{u}}) = \left(K + \frac{4}{3} \mu \right) \Delta (\nabla \cdot \mathbf{u}),$$

(2.19)

$$\rho (\nabla \times \ddot{\mathbf{u}}) = \mu \, \Delta (\nabla \times \mathbf{u}).$$

(2.20)

Equation (2.19) is the compression wave equation, which is a scalar equation for waves polarized parallel to the propagation direction. Equation (2.20) is the shear wave equation for waves with polarization perpendicular to the direction of travel. Both equations are satisfied by a plane wave

$$\mathbf{u}(\mathbf{r}, t) = \mathbf{u}_0 e^{i\omega \left(\frac{1}{c} \mathbf{n} \cdot \mathbf{r} - t \right)}$$

(2.21)

with $\mathbf{n}$ being the wave normal vector. c denotes the wave speed, which is

$$c = \sqrt{\frac{K + \frac{4}{3}\mu}{\rho}} \quad \text{for compression waves and} \tag{2.22}$$

$$c = \sqrt{\frac{\mu}{\rho}} \quad \text{for shear waves.} \tag{2.23}$$

Elastography measures the shear modulus of soft tissues by stimulating shear waves and using medical imaging such as ultrasound [8] or MRI [9]: to detect them. The investigated tissues are often considered incompressible, since compression modulus K is several orders of magnitude larger than shear modulus μ. However, true incompressibility implies both vanishing volumetric strain ($\nabla \cdot \mathbf{u} \to 0$) and infinitely high compression modulus ($K \to \infty$). Even though in incompressible media neither of the two parameters alone can be measured with sufficient precision, their product is finite and is identified as isotropic pressure:

$$p = -K\left(\nabla \cdot \mathbf{u}\right) = -\frac{1}{3}\left(\sigma_{11} + \sigma_{22} + \sigma_{33}\right). \tag{2.24}$$

Note that, due to the high content of water in biological soft tissues (>75%), the compression modulus does not vary much when the material behaves monophasically. Monophasic properties imply that all constituents of the tissue, including solid and fluid compartments, move in synchrony as one field. Biological soft tissues normally behave monophasically at high stimulation frequencies as in sonography (on the order of MHz). For this reason, the compression modulus measured by ultrasound can be approximated by the speed of sound in water (~1500 m/s), which corresponds to a compression wavelength of 1.5 mm at 1 MHz frequency. On the other hand, the frequency range of elastography, which is between 10 and 100 Hz in clinical applications, results in compression wavelengths on the order of 15–150 m, entailing a pressure gradient which does not vary in space, that is, $\nabla p = (K + 4/3\mu)\nabla(\nabla \cdot \mathbf{u}) = const$. Hence, Eq. (2.18) can be simplified for incompressible media to

$$\rho \ddot{\mathbf{u}} = \mu \Delta \mathbf{u} + const \tag{2.25}$$

by using the vector calculus identity $\Delta \mathbf{u} = \nabla(\nabla \cdot \mathbf{u}) - \nabla \times (\nabla \times \mathbf{u})$. Time-harmonic elastography usually solves Eq. (2.25) for shear modulus μ by direct inversion, phase gradient methods, or local frequency estimation [10] after suppressing the offset pressure term using spatial filters or the curl operator as in Eq. (2.20) [11]. In contrast, without assuming a constant pressure gradient, multiparameter recovery can yield both Lamé coefficients by either variational approaches [12–14] or direct inversion [15, 16].

Poroelastography explicitly aims at quantifying tissue pressure based on the hypothesis that the compression modulus in multiphasic media at low stimulation frequencies is much lower than predicted by ultrasound. A good example is the

brain: the speed of sound (compression waves) in ultrasound imaging of brain matter is, as in any other soft tissues, on the order of 1500 m/s, corresponding to a compression modulus of 2.2 GPa. In contrast, arterial pulsation causes cyclic brain expansion to an order of tens of milliliters, which can be observed by MRI as movement of tissue boundaries. The estimated compression modulus of the brain in this quasi-static dynamic range is on the order of only 26 kPa [17] highlighting the relevance of multiphasic models for understanding tissue compression in the static and quasi-static limit. Further details and applications are discussed in Chaps. 4 and 20.

2.4   Wave Scattering and Diffusive Waves

So far we have considered only unscattered plane waves which propagate along a straight line between two points. However, in heterogeneous media such as biological tissues, waves are typically scattered at elastic discontinuities, giving rise to a "smeared" wave intensity within the region through which the wave has passed. When traversing a scattering medium, the propagating wave front continuously loses amplitude since, at each single scattering event, wave intensity is split between the transmitted and reflected waves. Moreover, wave coherence in a global ensemble of stochastically scattered small wave packages is lost, causing a decrease in average wave amplitude. The most fundamental principle of wave scattering is that a wave changes direction when it hits an interface. This means that part of the wave is reflected while another part is transmitted through the interface. The two parts of the wave travel with different amplitudes into different directions. The change in amplitudes of scattered waves in 1D is derived in the following.

2.4.1   Wave Scattering at Planar Interfaces

The most basic wave scattering scenario is a plane incident wave orthogonally hitting an interface between two media with different elastic properties. In this scenario, the normal vector of the interface is parallel to the wave normal vector $\mathbf{n}$, and the polarization of the incident wave is preserved for the reflected and transmitted waves. We will therefore ignore the polarization vector in Eq. (2.21) and instead discuss a scalar 1D plane wave of amplitude u_0. Coordinate r identifies the position along the propagation direction of the wave. The elastic discontinuity is located at $r=0$, dividing the medium into two compartments, compartment 1 for $r<0$ and compartment 2 for $r>0$. Incident and reflected waves traverse 1, while the transmitted wave propagates through 2 (Fig. 2.4). We first define the transmission and reflection coefficients, T and R, as the amplitude of the transmitted ($u_{0(t)}$) and reflected ($u_{0(r)}$) wave at the boundary, normalized to the incident wave amplitude ($u_{0(i)}$):

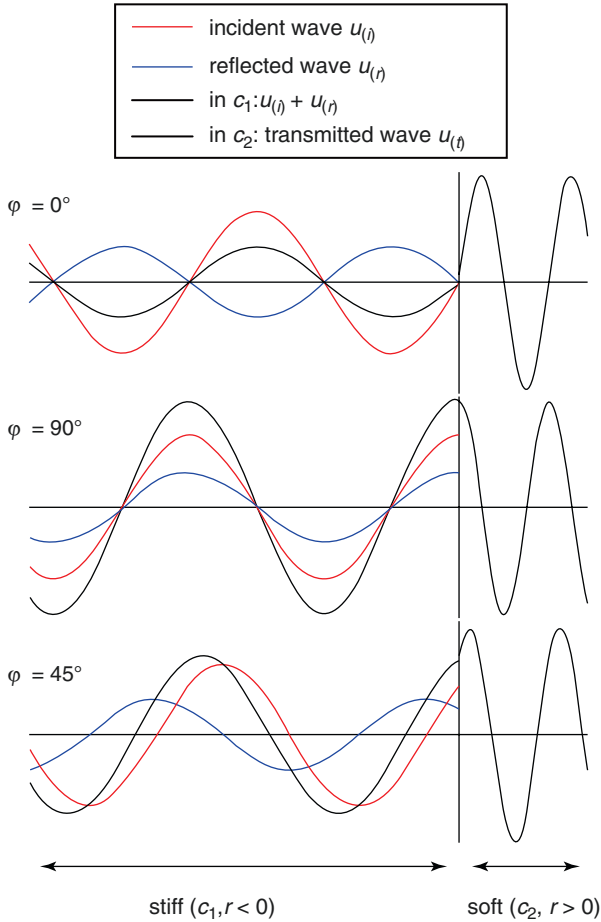$$T = \frac{u_{0(t)}}{u_{0(i)}}, \tag{2.26}$$

Fig. 2.4 1D wave scattering at an elastic interface at $r = 0$. The wave amplitudes on both sides of the interface are considered to be equal as implied by the boundary condition of Eq. (2.28) (nonslip condition). Shown are three different phases ϕ of the waves with respect to $r = 0$

$$R = \frac{u_{0(r)}}{u_{0(i)}}. \tag{2.27}$$

We assume nonslip conditions, i.e., 1 and 2 are in close contact, so that wave amplitudes in both compartments are equal at $r = 0$, which yields

$$u_{0(i)} + u_{0(r)} = u_{0(t)}$$
$$T - R = 1. \tag{2.28}$$

Furthermore, conservation of energy requires a continuous flux of wave energy through the interface in the steady state. Therefore, energy inflow equals energy outflow or

$$\left\langle \mathbf{P}_{(i)} \right\rangle = \left\langle \mathbf{P}_{(r)} \right\rangle + \left\langle \mathbf{P}_{(t)} \right\rangle. \tag{2.29}$$

$\left\langle \mathbf{P}_{(i)} \right\rangle$, $\left\langle \mathbf{P}_{(r)} \right\rangle$, and $\left\langle \mathbf{P}_{(t)} \right\rangle$ denote the time average of harmonic steady-state energy fluxes through the interface of incident, reflected, and transmitted waves, respectively. The flux vectors are obtained by combining Eqs. (2.15) and (2.21), such that

$$\left\langle P \right\rangle = \rho c^2 \frac{\partial u}{\partial r} \frac{\partial u}{\partial t} \quad \text{with} \quad u = \text{Re}\left[u_0 e^{i\omega\left(\frac{1}{c}r - t\right)} \right]. \tag{2.30}$$

Since energy is a scalar, real-valued quantity, we accounted for the real part of the complex wave (Re) hitting the interface at $r = 0$ (thus $\left\langle P \right\rangle$ denotes here the scalar flux amplitude). From the above equation, one obtains, for the average energy of each wave component,

$$\left\langle P_{(i)} \right\rangle = \frac{1}{2} \rho_1 c_1 u_{0(i)}^2, \tag{2.31}$$

$$\left\langle P_{(r)} \right\rangle = \frac{1}{2} \rho_1 c_1 u_{0(r)}^2, \tag{2.32}$$

$$\left\langle P_{(t)} \right\rangle = \frac{1}{2} \rho_2 c_2 u_{0(t)}^2, \tag{2.33}$$

with indices 1 and 2 for the respective compartments. Combining Eqs. (2.28)–(2.33) and solving for T and R results in the well-known scattering amplitude coefficients in 1D for perpendicular incidence:

$$T = \frac{2c_1\rho_1}{c_1\rho_1 + c_2\rho_2} \quad \left(\text{transmitted wave amplitude}\right), \tag{2.34}$$

$$R = \frac{c_1\rho_1 - c_2\rho_2}{c_1\rho_1 + c_2\rho_2} \quad \left(\text{reflected wave amplitude}\right). \tag{2.35}$$

When multiple interfaces (scatterers) are present and $R \neq 0$, wave amplitudes behind the wave front become speckled through constructive and destructive interferences of incident and reflected waves. In 2D and 3D, T and R depend on the direction cosines of incident and transmitted waves relative to the interface, rendering the amplitudes of the transmitted and reflected wave front direction dependent [18].

2.4.2 Stochastic Wave Scattering

Turning back to biological tissues characterized by a stochastic distribution of elastic discontinuities, we will further consider the superposition of many wave packages with individual effective propagation path lengths r. In this model, we assume a stochastic distribution of small scattering inclusions. If scatterer density is high enough, every voxel will contain a superposition of multiply scattered and transmitted partial waves with no well-defined phase relation between them. In other words, the wave amplitude in every voxel is defined by the interference of several waves with random amplitudes and phases.

Similar to diffusion, r would then represent the effective distance a wave package has reached. Hence, we find a distribution of effective wave speeds c defined by the effective distance r divided by waiting time t. However, contrary to diffusion, there is a maximum c-value which corresponds to the wave speed of the unscattered wave [11]. A wave front is defined by the most advanced wave components, since—as previously said—any scattering event is a deflection from a straight line of propagation and hence the effective distance the wave has traveled from the source is reduced, corresponding to a reduced effective wave speed. In other words, the wave front contains only the components that were transmitted at each single scattering event with relative amplitudes T. Assuming a uniform distribution of solid scatterers throughout the sample and thus a constant time interval τ_s between two scattering events, we can define the decrease in amplitude $u_0(t)$ by

$$u_0\left(t+\tau_s\right) = T\ u_0\left(t\right). \tag{2.36}$$

For sufficiently small intervals τ_s, one can represent $u_0(t+\tau_s)$ by the first order of the Taylor series around t:

$$u_0\left(t+\tau_s\right) \approx u_0\left(t\right)+\dot{u}_0\left(t\right)\ \tau_s. \tag{2.37}$$

Combining the right-hand sides of these two equations yields

$$\dot{u}_0\left(t\right) = \frac{T-1}{\tau_s}u_0\left(t\right)$$

$$\Rightarrow u_0\left(t\right) = u_0\left(t=0\right)\ e^{-\frac{1-T}{\tau_s}t}. \tag{2.38}$$

The unscattered wave front therefore decays exponentially with time at a rate of $-(1-T)/\tau_s = R/\tau_s$ and, since propagation velocity is constant, exponentially with the distance from the source. $u_0(t=0)$ is the wave amplitude at the source, which is switched on at $t=0$. Note that the wave amplitude of a wave front decreases even in nonabsorbing materials. However, the intensity of scattered waves is not lost but concentrated in the area "behind" the wave front. In this region, superposition of

multiply scattered waves occurs, giving rise to constructive and destructive interferences, which appear in ultrasound images as speckles. Overall wave intensity (energy) in our object is not affected by elastic scattering as long as no viscous damping occurs. Viscous damping, similar to diffusion, is a spontaneous irreversible process characterized by an increase in entropy. In contrast, elastic wave transport is reversible, which is reflected by the symmetry of the wave equation (second-order derivatives in time and space). As a consequence, time reversal of propagating waves is feasible and has already been used in medical imaging and therapeutic applications of ultrasound [19]. In contrast, photoacoustic tomography as detailed in Chap. 13 basically relies on optical energy absorption but is influenced by optical scattering processes. Despite the principal differences between diffusion equation and wave equation, both can be mathematically combined to obtain a very compact and elegant description of dispersive wave transport as outlined in the following section.

2.4.3 Wave Diffusion and Scale-Free Viscoelastic Properties

The diffusion equation (2.4) and the wave equation as given in Eq. (2.19) or Eq. (2.20) can be regarded as just two special cases of a more general description of wave diffusion. An equilibrium equation which fulfills the two limits of diffusion and unattenuated waves is obtained utilizing a fractional derivative operator α:

$$\rho \frac{\partial^{2-\alpha} \mathbf{u}}{\partial t^{2-\alpha}} = \kappa \Delta \mathbf{u}, \text{ with } 0 < \alpha \leq 1. \tag{2.39}$$

$\alpha = 1$ and $\kappa = \rho D$ apply for pure diffusive particle motion, while $\alpha = 0$ and $\kappa = \rho c^2$ for unattenuated waves. A general treatment of fractional derivative operators is beyond the scope of this review. We instead refer to the literature of fractional calculus for general problems in diffusion and viscoelasticity such as [20]. For harmonic functions, the Weyl definition of the fractional derivative operator yields the following linear relationship between the Fourier transform (*FT*) and derivatives [21]:

$$FT\left[\frac{\partial^{\alpha} f(t)}{\partial t^{\alpha}}\right] = (i\omega)^{\alpha} FT\left[f(t)\right]. \tag{2.40}$$

Thus, for time-harmonic waves in the frequency domain $\tilde{\mathbf{u}}(\omega)$, Eq. (2.39), the following wave equation is obtained:

$$\rho FT\left[\frac{\partial^{2-\alpha} \mathbf{u}(t)}{\partial t^{2-\alpha}}\right] \Rightarrow \rho (i\omega)^{2-\alpha} \tilde{\mathbf{u}}(\omega) = -\frac{\rho \omega^2}{(i\omega)^{\alpha}} \tilde{\mathbf{u}}(\omega). \tag{2.41}$$

Correspondingly, the Laplacian of a time-harmonic wave as defined in Eq. (2.21) gives

$$\kappa \; FT\big[\Delta \mathbf{u}(t)\big] \Rightarrow -\kappa \frac{\omega^2}{c^2} \tilde{\mathbf{u}}(\omega). \tag{2.42}$$

Combining Eqs. (2.41) and (2.42) yields

$$\rho c^2 = \kappa (i\omega)^{\alpha} \equiv G^*(\omega). \tag{2.43}$$

We here defined the complex-valued modulus $G^*(\omega)$, the real part of which is the storage modulus that governs the elastic properties of a material, while the imaginary part is the loss modulus that quantifies viscous properties. Equation (2.43) illustrates that transition from non-damped waves to diffusive waves is associated with loss of wave energy due to loss of phase coherence, which is equivalent to viscous attenuation as usually described in viscoelastic theory by viscoelastic models based on springs and dashpots. The combination of the two as defined in Eq. (2.43) is the *springpot*. Notably, the springpot is a power law with the same exponent α for both the real and imaginary parts of $G^*(\omega)$, meaning that the ratio between loss and storage properties is constant over frequency. If a material shows a constant ratio between viscous and elastic properties over a wide range of frequencies, the material is considered to be scale-free, meaning that viscoelastic properties measured at the macroscopic scale of typical medical imaging resolutions can be directly translated into much smaller dimensions, such as the cellular scale, by means of a hierarchical network with only two parameters κ and α [22]. The springpot predicts a constant loss angle δ, which quantifies the ratio between viscous and elastic properties:

$$\delta = \arctan\left(\frac{\mathrm{Im}\big[G^*(\omega)\big]}{\mathrm{Re}\big[G^*(\omega)\big]}\right) = \alpha \frac{\pi}{2}. \tag{2.44}$$

Note that κ in Eq. (2.43) has a cumbersome dimension, which depends on the value of α. Therefore, in the literature, κ is usually converted to an elastic modulus by $\kappa = \mu^{1-\alpha}\eta^{\alpha}$ comprising a shear modulus μ and shear viscosity η. To derive μ from κ requires assumptions on η. In the literature, η is often set to unity, to 3.7 Pa·s for brain tissue, or 7.3 Pa·s for liver tissue [23]. Springpot-based viscoelastic dispersion functions are shown in comparison to other two-parameter models of viscoelasticity in Fig. 2.5. Experimental data demonstrate that the springpot is widely applicable to describe viscoelastic properties of biological soft matter [22, 23]. It is an intriguing observation that we arrived at the springpot-related properties of biological tissues starting with the diffusion-wave equation (Eq. (2.39)). This further highlights that a mixed description of coherent and incoherent wave transport phenomena applies to biological soft tissues.
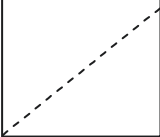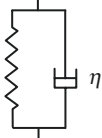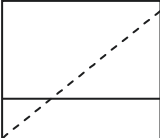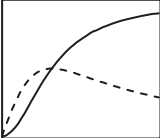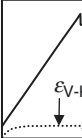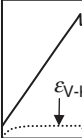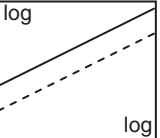
K-V Model	Schematic	Modulus G^*	$G'(\omega)$ $\mathrm{Re}G^*(\omega)$ —— $G''(\omega)$ $\mathrm{Im}G^*(\omega)$ - - -	$\varepsilon(t)$
spring (Hookean)	μ	μ		
dashpot (Newtonian)	η	$\eta i\omega$		
Kelvin-Voigt (K-V)	μ η	$\mu + \eta i\omega$		
Maxwell	μ η	$\dfrac{\mu\eta i\omega}{\mu + \eta i\omega}$		$\varepsilon_{V\text{-}K}$
Springpot	μ, η, α	$\mu^{1-\alpha}\eta^{\alpha}(i\omega)^{\alpha}$ $(0 \leq \alpha \leq 1)$	log $\qquad$ log	$\alpha = 0.5$ $\alpha = 0.25$

Fig. 2.5 Basic elements, spring and dashpot, which model the elastic and viscous response of a material and are used to assemble two-parameter viscoelastic models as sketched in the second column. Complex modulus G^* for the shown models is analytically given in the third column and schematically plotted in the fourth column over angular frequency (G' and G'' denote the storage and loss modulus, respectively). "log" refers to double logarithmic plots to better illustrate the power law behavior of the springpot. The rightmost column shows strain $\varepsilon(t)$ on a time axis in response to a boxcar stress spanning the first half of the time axis

2.5 Flow-Related Transport

Flow comprises many length scales in living tissue, ranging from large-distance-directed blood flow to microperfusion through stochastically distributed capillaries, where flow is similar to diffusive motion. The mathematical description of flow phenomena is similar to that of waves; however, since flow involves transport of

mass rather than energy, convection has to be taken into account. Most fluids cannot store shear strain energy due to their property of moving along an acting stress without generating a resistive force. Therefore, shear stress in fluids exists only in its viscous form, which is proportional to strain rate. In the previous section, we already introduced viscoelasticity based on the two-parameter springpot model. The two other models with only two independent parameters are the Voigt and Maxwell models, which represent parallel and serial arrangements of a spring- and a dashpot, respectively [11]. In the Voigt model, total stress is the sum of two partial stresses corresponding to spring and dashpot, whereas in the Maxwell model, total strain is the sum of the two partial strains. A simple extension of Hooke's law given in Eq. (2.8) to include a viscosity tensor is

$$\boldsymbol{\sigma} = \mathbf{C}_{\text{elastic}} \cdot \boldsymbol{\varepsilon} + \mathbf{C}_{\text{viscous}} \cdot \dot{\boldsymbol{\varepsilon}}. \tag{2.45}$$

$\dot{\boldsymbol{\varepsilon}}$ is the strain-rate tensor. As stated before, since fluids do not respond elastically to shear deformation, all shear-related entries of $\mathbf{C}_{\text{elastic}}$ are zero. However, it is important to note that even purely viscous materials with respect to shear can still respond elastically to compression, resulting in an isotropic pressure p. Furthermore, viscosity induces a rate-dependent resistance to shear deformation, even if there is no elastic response. We therefore reduce the elastic stress to its compression elements ($\nabla \cdot \mathbf{u}$), while the full viscous stress tensor is retained [24]:

$$\boldsymbol{\sigma} = \left[\left(K - \frac{2}{3}\mu \right) (\nabla \cdot \mathbf{u}) + \left(\varsigma - \frac{2}{3}\eta \right) (\nabla \cdot \dot{\mathbf{u}}) \right] \mathbf{I} + \eta \dot{\boldsymbol{\varepsilon}}. \tag{2.46}$$

ς denotes compression viscosity, whereas η is shear viscosity (both in units Pa·s). By addressing motion of incompressible fluids such as blood, we can collapse both divergence terms in Eq. (2.46) into a single pressure parameter similar to pressure in incompressible elastic solids:

$$\boldsymbol{\sigma} = -p\mathbf{I} + \eta \dot{\boldsymbol{\varepsilon}}. \tag{2.47}$$

Here, p is a lumped pressure parameter that combines volumetric strain and volumetric strain rate. Both volumetric strain terms are evanescent in the limit of incompressibility, while compression modulus K and compression viscosity ς become infinitely large, resulting in p as a nonkinetic stress quantity which depends neither explicitly on strain nor strain rate. However, since p can vary in space, this parameter remains part of the equilibrium equation as shown below.

So far, we have accounted for viscous damping and have eliminated the shear strain from $\boldsymbol{\sigma}$. A further distinction between solid and fluid motion is the coordinate system relative to which displacements are measured. In a solid medium, each particle is very much restricted in its range of motion and can only undergo very small deflections from its equilibrium position. The strain field is therefore a measure of the deflection of each mass point, as seen from the static coordinate system that defines the equilibrium state. This point of view is also referred to as the *Eulerian* description. In fluids, on the other hand, mass can be deflected by an arbitrary

amplitude from its original position due to the lack of a restoring force. Particle deflections are therefore not small but can accumulate in an unconstrained fashion over time. It is therefore more common to use the *Lagrangian* description, which moves along the trajectory $\mathbf{r}(t)$ of the flowing medium [25]. Consequently, a fluid displacement field $\mathbf{u}$ can be parameterized by $\mathbf{u}(\mathbf{r}(t), t)$, which is the motion around equilibrium position plus motion of the coordinate system. In this case, the temporal derivative has to be calculated as an absolute derivative (also called *material deriva-tive*) [1]:

$$\frac{d\mathbf{u}}{dt} = \frac{\partial \mathbf{u}}{\partial t} + \frac{\partial \mathbf{r}}{\partial t} \cdot \nabla \mathbf{u} = \left(\frac{\partial}{\partial t} + \mathbf{v} \cdot \nabla \right) \mathbf{u}. \tag{2.48}$$

$\mathbf{v} = \dfrac{\partial \mathbf{r}}{\partial t}$ denotes the velocity of the material's coordinate system in which any local property change occurs. In contrast to the Eulerian description that only quantifies displacement from a reference position, as caused by propagating (pressure) waves, Eq. (2.48) incorporates the flow-related aspect of convection, which comprises the trajectory of the flow as well as boundary effects, such as the acceleration of flow in a funnel. The parameter measured in flow imaging is flow velocity $\mathbf{v}$. The equilibrium equation of a flow field $\mathbf{v}$ is obtained from the continuity equation (2.1) similar to Newton's second law, which, above, led us to Navier equation (2.16). Combining the material derivative from Eq. (2.48) with Eq. (2.16) leads to

$$\rho \left(\dot{\mathbf{v}} + \mathbf{v} \cdot \nabla \mathbf{v} \right) = \nabla \cdot \boldsymbol{\sigma}. \tag{2.49}$$

The Navier-Stokes equation for incompressible fluids is readily obtained by inserting fluid stress tensor $\boldsymbol{\sigma}$ of Eq. (2.47) into Eq. (2.49):

$$\rho \left(\dot{\mathbf{v}} + \mathbf{v} \cdot \nabla \mathbf{v} \right) = -\nabla p + \eta \Delta \mathbf{v}. \tag{2.50}$$

The Navier-Stokes equation plays a central role in medical imaging of fluid dynamics since it fully describes the evolution of flow stream lines depending on the geometry and elasticity of the vessel pipelines as well as the distribution of pressure within the cardiovascular system. Flow imaging by Doppler ultrasound is of utmost importance for the clinical diagnosis of vascular dysfunctions in many organs [26]. Phase-contrast (PC) MRI has extended the knowledge of blood flow in the cardio-vascular system in health and disease [27]. The strength of flow PC-MRI is to pro-vide three-dimensional vector fields of $\mathbf{v}$ (and acceleration terms $\dot{\mathbf{v}}$) with good spatiotemporal resolution, enabling researchers to model flow by implementing dif-ferent boundary conditions into the Navier-Stokes equation and to solve it by numerical methods. There is no general solution to the Navier-Stokes equation due to the convective term $(\mathbf{v} \cdot \nabla \mathbf{v})$ on the left-hand side of Eq. (2.50), which makes it nonlinear and difficult to handle without a priori assumptions on boundary values. As an example, if an incompressible fluid flowing through a thick pipe is funneled into a pipe of smaller diameter, this can only be achieved if the fluid is accelerated. Hence, there is an acceleration term that is caused by the geometric properties of the boundaries, which cannot be derived from the acting forces alone. In contrast, waves

can be focused or defocused (e.g., by the source geometry) without affecting their propagation velocity but only their amplitudes. Further details on the numerical treatment of the Navier-Stokes equation for cardiovascular MRI as well as PC-MRI experiments are provided in Chaps. 3 and 9.

2.6 Perfusion

Perfusion is blood flow at the capillary level and is closely related to the delivery of oxygen and other nutrients to the tissue [28]. Hence, perfusion is linked to the metabolism of the tissue, which can change tremendously in the presence of diseases such as tumors or ischemia. For this reason, perfusion has been used as a clinical imaging marker in CT, MRI, sonography, PET, and SPECT for a long time. Perfusion can be measured using either exogenously administrated tracers or intrinsically labeled particles based on their change in concentration within the targeted tissue. This means that perfusion measurement can be seen as the measurement of the concentration $C(t, \mathbf{r})$ of any kind of labeled particles over time. Common labeling methods include radioactive tracers (PET, SPECT), magnetically labeled proton spins (arterial spin labeling MRI, ASL-MRI), paramagnetic contrast agents (dynamic susceptibility contrast MRI), radiation-absorbing agents (CT), or contrast agents based on gas bubbles (sonography). During the first phase of particle inflow, the tracer concentration rises with arrival in the arteries, which is followed by a second phase during which the tracer concentration decreases due to washout. Mechanisms for tracer washout include diffusion from the vascular bed into the tissue, venous drainage, and a combination of both. Perfusion falls into the range between flow and diffusion: on the one hand, tracers are delivered by the instreaming blood, which is a coherent transport mechanism. On the other hand, random distribution of the transport pipelines or diffusion of the tracers from the blood into the tissue can result in a diffusive decay of the measured signals. Hence, we have to account for both tracer density ρ and blood velocity $\mathbf{v}$ variation in space and time, resulting in the perfusion flux vector

$$\mathbf{P}(\mathbf{r},t) = \rho(\mathbf{r},t)\mathbf{v}(\mathbf{r},t). \tag{2.51}$$

The divergence of the flux in the continuity equation (2.1) readily follows as

$$\frac{\partial \rho}{\partial t} = -(\nabla \rho) \cdot \mathbf{v} - \rho \nabla \cdot \mathbf{v}. \tag{2.52}$$

We note that the divergence of the flow field in the blood is nearly zero ($\nabla \cdot \mathbf{v} = 0$) due to incompressibility as discussed above.

For the following discussion, we assume that uptake of nutrients and tracers occurs only at the smallest scale of vascular hierarchy, marking the transition from the arterial to the venous tree. We denote the "thickness" of this zone by L (see Fig. 2.2) and approximate the concentration gradient with a finite difference. We also substitute density ρ in Eq. (2.52) with a concentration $C(t, \mathbf{r})$ [29]:

$$\frac{\partial C}{\partial t} = -\nabla C \cdot \mathbf{v} = \frac{C_a - C_v}{L} \cdot \frac{L}{\Delta t}. \tag{2.53}$$

Here, the spatial gradient of $C(t, \mathbf{r})$ is approximated by the difference between local concentration of tracers in arteries and veins, $C_a(t)$ and $C_v(t)$, respectively; hence $C(t, \mathbf{r}) \Rightarrow C(t)$. This implicitly assumes that the concentration predominantly changes along the direction of the path from arteries to veins. Δt is the time that the tracer requires to transit the exchange zone. Unlike flow imaging, which quantifies blood flow velocities, perfusion usually measures blood flow (BF) as a scalar parameter, which is blood volume (ml) per transport time (minutes) normalized to tissue mass (100 g). However, while the decay rate $(1/\tau)$ of the tracer signal is the actual measure of perfusion, the blood volume per tissue mass is normally not known. Instead, assumptions have to be made to calibrate the initial rate of perfusion to BF [30]. τ is identified as the mean transit time, which is the time a certain volume of blood (BV) spends in the capillary circulation, i.e., $\tau = BV/BF$. Using τ we can rewrite Eq. (2.53) to obtain the equilibrium equation of perfusion:

$$\frac{d\bar{C}(t)}{dt} = \frac{1}{\tau}\left(C_a(t) - C_v(t)\right). \tag{2.54}$$

$\bar{C}(t)$ is the tracer concentration averaged over the exchange region. A common assumption is $C_v(t) = \lambda \bar{C}(t)$, with $\lambda < 1$ [29]. Partition coefficient λ quantifies the retention of a tracer by the tissue. Delay of washout can be effected by various mechanisms including diffusion of the tracers from the blood into the tissue (diffusible tracers) or by circulation inside the blood pool (blood pool agent). The differential equation

$$\frac{d\bar{C}(t)}{dt} = \frac{1}{\tau}\left(C_a(t) - \lambda \bar{C}(t)\right) \tag{2.55}$$

is solved with

$$\bar{C}(t) = \left(\int \frac{C_a(t)}{\tau} e^{\frac{t}{\lambda \tau}} dt + A\right) e^{-\frac{t}{\lambda \tau}}. \tag{2.56}$$

Further assumptions about the arterial input function $C_a(t)$ are necessary to solve the integral and to specify A. The scenario of a transient tracer bolus that arrives at $t = t_0$ with concentration C_0 can be modeled by a Dirac function

$$C_a(t) = C_0 \delta(t - t_0). \tag{2.57}$$

This, combined with the initial condition of $\bar{C}(t = 0) = 0$, yields an exponential decay of tracer particle concentration over time with the perfusion rate $1/(\tau \lambda)$,

$$\bar{C}(t) = \frac{C_0}{\tau} \Theta(t - t_0) e^{-\frac{t}{\tau \lambda}} \text{ with } \Theta \to \begin{cases} 0: & t < t_0, \\ 1: & t \geq t_0, \end{cases} \tag{2.58}$$

Table 2.1 Diffusion—perfusion—flow—waves: mass and energy transport quantified by medical imaging modalities

Transport mechanism	Continuity equation	Flux	Equilibrium equation	Solution
Diffusion	$\dot{\rho} = -\nabla \cdot \mathbf{P}$	$\mathbf{P} = -D\nabla\rho$	$\dot{\rho} = D\Delta\rho$	$N(r,t) = \dfrac{1}{\left(4\pi Dt\right)^{\frac{3}{2}}} e^{-\frac{r^2}{4Dt}}$
Elastic waves	$\dot{E} = -\nabla \cdot \mathbf{P}$	$\mathbf{P} = -\boldsymbol{\sigma} \cdot \dot{\mathbf{u}}$ $\boldsymbol{\sigma} = \mathbf{C}_{\text{elastic}} \cdot \boldsymbol{\varepsilon}$	$\rho\ddot{\mathbf{u}} = \left(K + \dfrac{4}{3}\mu\right)\nabla\left(\nabla \cdot \mathbf{u}\right)$ $- \mu\nabla \times \left(\nabla \times \mathbf{u}\right)$	$\mathbf{u} = \mathbf{u}_0 e^{i\omega\left(\frac{1}{c}\mathbf{n}\cdot\mathbf{r}-t\right)}$ $\rho c^2 = K + \dfrac{4}{3}\mu$ (compression waves) $\rho c^2 = \mu$ (shear waves)
Diffusive waves	--	--	$\rho \dfrac{\partial^{2-\alpha}\mathbf{u}}{\partial t^{2-\alpha}} = \kappa\Delta\mathbf{u}$	$\kappa = \rho D$, for $\alpha = 1$ (diffusion) $\kappa = \mu$, for $\alpha = 0$ (elastic waves) $\kappa = \mu^{1-\alpha}\mu'^{\alpha}$, for $0 < \alpha < 1$ (diffusive waves)
Flow[a]	$\dot{E} = -\nabla \cdot \mathbf{P}$	$\mathbf{P} = -\boldsymbol{\sigma} \cdot \mathbf{v}$ $\boldsymbol{\sigma} = \mathbf{C}_{\text{elastic}} \cdot \boldsymbol{\varepsilon}$ $+ \mathbf{C}_{\text{viscous}} \cdot \dot{\boldsymbol{\varepsilon}}$	$\rho\left(\dot{\mathbf{v}} + \mathbf{v} \cdot \nabla\mathbf{v}\right) =$ $-\nabla p + \eta\Delta\mathbf{v}$	–
Perfusion	$\dot{C} = -\nabla \cdot \mathbf{P}$	$\mathbf{P} = -C\ \mathbf{v}$	$\dot{C}(t) = \dfrac{1}{\tau}\begin{pmatrix} C_a(t) \\ -\lambda C(t) \end{pmatrix}$	$C(t) = \dfrac{C_0}{\tau}\Theta\left(t - t_0\right)e^{-\frac{t}{\tau\lambda}}$

[a]Incompressible fluids

where $\Theta(t - t_0)$ denotes the Heaviside function. A more detailed analysis needs to account for specific input functions $C_a(t)$ which can simulate the experimentally observable finite increase in arterial concentrations over time.

In perfusion MRI, the blood is magnetically labeled (arterial spin labeling, ASL) right before entering the imaging volume. After a delay time, an image is acquired, in which the presence of labeled blood reduces image intensity relative to an unlabeled reference image. The delay between labeling and image acquisition corresponds to the delay time t_0 in Eq. (2.58) (see Sect. 2.7.4 and Chap. 22 for a more detailed description of perfusion MRI).

Due to the hierarchy of the vascular architecture, delay time t_0 determines the range of sensitivity of the perfusion technique. During the delay between labeling and image acquisition, the labeled blood is allowed to reach the capillaries, where it gives rise to the measured perfusion signal. Consequently, shorter waiting times

shift the sensitivity of perfusion measurements toward arteriole perfusion when the blood has not yet entered the capillary bed.

A summary of the equations governing mechanical and transport-related parameters as quantified by medical imaging is given in Table 2.1.

2.7   Motion Encoding by Medical Imaging

Measurement of motion by medical imaging modalities requires encoding of tissue deflection or particle velocity into the image contrast or labeling part of the tissue (e.g., blood or water) in a series of time-resolved images. The latter approach was the initial way of motion measurement by medical imaging and is referred to as *bolus tracking*. Bolus tracking is used in almost all medical imaging methods including CT, MRI, PET, and ultrasound. For example, CT angiography uses an injection of iodine-based contrast agents to help diagnose and evaluate blood vessel disease or related conditions, such as aneurysms or steno-occlusive disease. Similarly, in MRI, either gadolinium-based contrast agents or manipulation of the proton spin magnetization are used to enhance image contrast. For instance, in arterial spin labeling, the transverse spin magnetization of instreaming blood is changed by radiofrequency pulses, allowing the measurement of signal intensity variations related to flow and perfusion without employing a contrast agent [30].

2.7.1   Motion Encoding in Medical Ultrasound

An important principle of motion encoding in ultrasound relies on the Doppler effect. If an ultrasound wave with a given frequency f scatters at moving tissue boundaries or blood particles, it undergoes a frequency shift twice: first when the moving particle acts as a receiver of an incident wave and a second time when the particle emits the wave as a moving source. The overall frequency shift is

$$\Delta f = \frac{c + v_a}{c - v_a} f \approx \left(1 + \frac{2v_a}{c} \right) f.$$

(2.59)

v_a is the velocity of the signal-emitting particle in the direction of the ultrasound beam (axial direction, with positive values indicating motion toward the ultrasound probe), and c is the ultrasound wave speed in the tissue [26]. Thus, measuring the frequency shift Δf allows the calculation of v_a, which, however, is not the true particle velocity but its projection onto the ultrasound beam axis. Therefore, v_a is usually corrected for the projection angle enclosed by the vessel (flow direction) and the ultrasound beam. Δf is easy to measure from a continuous wave source but extremely difficult to determine from a pulsed source. Normal ultrasound mode is pulsed since short wave packages offer higher spatial resolution. However, the lower the number of ultrasonic wave cycles in a pulse, the higher the uncertainty of Doppler frequency estimation due to decreased frequency resolution. Therefore,

Doppler methods rely on a trade-off between continuous and pulsed waves, which inherently limits both spatial resolution and the accuracy of frequency estimation. Additional limitations of measuring Δf arise from physical processes including viscous damping and frequency-dependent scattering, which can also modulate the frequency of the received signal.

Therefore, many motion-encoding modes in ultrasound rely on correlation techniques termed *color mode* [26]. In the color mode, the ultrasound signals of two lines acquired at different times are correlated with each other. Axial resolution is achieved by successively shifting the correlation window along the signal line. Typical cross-correlation methods analyze the time shift or the phase shift of the ultrasound waves. Axial displacement u can be obtained from the maximum of the correlation function between two ultrasound wave signals $y_1(x,t)$ and $y_2(x, t+\Delta t) \approx y_1(x-u,t)$, i.e.,

$$\max_u \int y_1(x,t) y_2(x+u, t+\Delta t) \, dx. \tag{2.60}$$

The displacement then is the value of u which corresponds to the maximum of correlation. Since time Δt has passed between the acquisition of the two ultrasound lines, the measured quantity is velocity $u/\Delta t$. An alternative approach to motion estimation by ultrasound is the phase-shift method which exploits the phase shift $\Delta\phi(u)$ of the ultrasound wave due to displacement. If the axial distance between a particle and the ultrasound probe changes by an amount u between two acquisitions, the propagation path of the ultrasonic pulse from the probe to the particle and back to the probe changes by $2u$. The second pulse is thus detected with a phase offset $\Delta\phi = 2\pi \dfrac{2u}{\lambda} = 4\pi \dfrac{uf}{c}$, where λ is the ultrasonic wavelength. The phase offset $\Delta\phi(u)$ between two complex-valued signals $y_1(x,t) \propto \exp(i[kx+\phi_1])$ and $y_2(x, t+\Delta t) \propto \exp(i[kx+\phi_2])$ is obtained by the argument function [31]:

$$\Delta\phi = \phi_1 - \phi_2 = \arg\left(\frac{y_1}{y_2}\right). \tag{2.61}$$

For velocity measurements within larger two-dimensional regions, 2D correlation techniques such as *speckle tracking* can be used [32]. Despite their random nature, speckles in the ultrasound image display characteristic patterns of the tissue of interest and can thus be used to track motion. It has to be mentioned that, in general, ultrasound is limited in measuring lateral motion as compared to its high-resolution capabilities for motion tracking along the axial direction. Full 3D motion fields are still better acquired by MRI.

2.7.2 Motion Encoding in MRI

One of the most elaborate medical imaging technologies for motion quantification is MRI.

Motion can be encoded in the phase information of the complex magnetization exploiting frequency differences due to displacements of moving spins during application of magnetic field gradients [33]. Motion-sensitive MRI methods have many applications in medical diagnosis and research. Therefore, we will briefly review the motion-encoding mechanism that is used in MRI to detect and quantify coherent and incoherent motion.

Most biological tissues contain water molecules and thus a high number of hydrogen protons. In the presence of a static magnetic field, B_0, the magnetic moment associated with the spin of protons results in a macroscopic net magnetization, which forms the basis of MRI. In particular, the signal in MRI is based on the excitation of transverse magnetization relative to B_0 by means of resonant radiofrequency (RF) pulses. Directly after excitation of such magnetization, all spin ensembles precess about the direction of the main magnetic field with precession frequency ω_0. Spin ensembles or particles with the same precession frequency are called *isochromats*. ω_0 is also known as the Larmor frequency and depends on the magnetic field strength:

$$\omega_0 = \gamma B_0, \tag{2.62}$$

where γ denotes the gyromagnetic ratio of protons ($\gamma = 2\pi\, 42.58$ MHz/T). In MRI, the local precession frequency is modulated by applying linear magnetic field variations in space, which are referred to as "gradients" $\mathbf{G}$, introducing the dependence of the resonance frequency of magnetization on the position $\mathbf{r}_0$:

$$\omega_{MRI}\left(\mathbf{r}_0\right) = \omega_0 + \gamma\, \mathbf{G} \cdot \mathbf{r}_0. \tag{2.63}$$

Quadrature detection implemented in the scanner hardware subtracts ω_0 from the resonance frequency, leaving the MRI signal in the rotating frame, i.e., $\omega'_{MRI}\left(\mathbf{r}_0\right) = \gamma\, \mathbf{G} \cdot \mathbf{r}_0$. ω'_{MRI} is the basic signal exploited by spatial frequency encoding in MRI. The phase of this signal accumulated during a time interval τ when a constant gradient $\mathbf{G}$ is deployed is

$$\varphi\left(\mathbf{r}_0, \tau\right) = \gamma\, \mathbf{G} \cdot \mathbf{r}_0 \tau. \tag{2.64}$$

This fundamental MRI phase equation is the basis for spatial encoding along the phase-encode axis (see Chap. 8), MRI motion encoding (see Chap. 9), as well as T_2^* mapping (see Chap. 15). We now assume the signal-emitting particles (e.g., blood or tissue) to move, so that their positions become time dependent. Furthermore, we account for time-varying gradients, e.g., a rectangular waveform of duration τ that changes polarity at $\tau/2$, i.e., a balanced bipolar gradient. Equation (2.64) then becomes

$$\varphi\left(\mathbf{r}_0, \tau\right) = \gamma \int_0^\tau \mathbf{G}(t) \cdot \left[\mathbf{r}_0 + \mathbf{r}(t)\right] dt. \tag{2.65}$$

$\mathbf{r}(t)$ is the trajectory of the isochromats around equilibrium position $\mathbf{r}_0$. This equation expresses the motion sensitivity of MRI conveyed by the phase of magnetization. For coherent motion phenomena, such as flow or tissue oscillations, where all

isochromats move more or less in synchrony (i.e., coherent) with their neighbors, φ is a good estimate of the ensemble spin phase in a voxel (i.e., the phase of the complex sum of all spins in that voxel). Therefore, coherent motion encoding by phase-contrast MRI based on Eq. (2.65) is the method of choice for flow field or wave field detection. Expanding the trajectory $\mathbf{r}(t)$ to the first order ($\mathbf{r}(\tau) \Rightarrow \mathbf{r}_0 + \dot{\mathbf{r}}\tau$) and assuming a rectangular gradient of total duration τ that is switched on for $0 \leq t \leq \tau$ yields for the accumulated spin phase

$$\varphi(t \geq \tau) = \gamma\,\mathbf{m}_0(\tau) \cdot \mathbf{r}_0 + \gamma\,\mathbf{m}_1(\tau) \cdot \dot{\mathbf{r}}_1, \tag{2.66}$$

with the zeroth- and first-order gradient moments $\mathbf{m}_0$ and $\mathbf{m}_1$. The n-th gradient moment is defined as

$$\mathbf{m}_n(\tau) = \int_{-\infty}^{\tau} \mathbf{G}(t) \cdot t^n dt. \tag{2.67}$$

A unipolar rectangular gradient has $\mathbf{m}_0(\tau) = \mathbf{G}\tau$ and $\mathbf{m}_1(\tau) = \frac{1}{2}\mathbf{G}\tau^2$, whereas a balanced bipolar rectangular gradient has $\mathbf{m}_0(\tau) = 0$ and $\mathbf{m}_1(\tau) = \mathbf{G}\tau^2$ [33] (more details on gradient moments are provided in Chap. 9). The zeroth-order term in Eq. (2.66) vanishes when bipolar gradients are applied leading to spin phase $\varphi = \gamma\mathbf{G} \cdot \mathbf{r}\tau = \gamma\,g\,r\,\tau$. g and r denote gradient amplitude and effective path length that the magnetization has traveled in the direction of gradient $\mathbf{G}$ during time τ, respectively. For flow, the resulting phase is therefore a measure of how far the magnetization has traveled between the application of the two gradient lobes and is thus proportional to the velocity.

2.7.3   Diffusion-Weighted MRI

In diffusion-weighted MRI, magnetization due to water molecules is labeled by imposing a phase that depends on the position of the magnetization along an axis that is defined by the direction of a magnetic *diffusion gradient* field [34].

The technique for motion encoding in MRI was explained in the previous section. However, diffusion represents an incoherent type of motion, and isochromats with different initial positions and motion trajectories are mixed within a voxel. In particular, we can imagine that the first lobe of a bipolar gradient produces a certain concentration of phase-labeled spins in each voxel, where the phase value depends on the position of the voxel along the direction of the gradient. Then the isochromats are allowed to perform random walk motion over a given evolution time before the spin phases are rephased by the second part of the diffusion gradient with opposite polarity. Signal-emitting particles that have moved randomly between the application of the two gradients result in phase dispersion, i.e., their magnetization vectors will partly cancel. This destructive interference is proportional to the distance that the particles have moved in the gradient direction (see Eq. (2.65)). The farther the particles in one voxel have traveled randomly, the more decorrelated their phases,

and thus the smaller the complex sum of all magnetization portions in the voxel, which constitutes the MRI signal. The relative strength of the signal in one voxel, compared to the signal obtained from an identical scan but without diffusion gradients, represents a measure of the *apparent diffusion coefficient* (ADC), which is the main parameter measured in diffusion-weighted MRI. The ADC indicates that the diffusion process is not free in tissues, can involve multiple compartments, and may be superposed by intra-voxel incoherent motion such as blood flow in small vessels or cerebrospinal fluid in ventricles, which also contribute to MRI signal attenuation. For brevity, we restrict our further discussion to D and calculate the loss of signal due to spin phase decorrelation by diffusion based on the Gaussian distribution for diffusive spin motion, described by Gaussian distribution $N(r,t)$, given in Eq. (2.5). As the simplest case, we analyze a bipolar pair of short diffusion gradients with amplitude g, duration τ, and temporal separation τ_Δ, as shown in Fig. 2.6a. We assume that the gradients are short enough that the spins can be assumed to be static while the gradients are applied. Under these conditions, Eq. (2.65) becomes $\varphi(r) = -\gamma g \tau r$, with r the distance by which the spin moves along the gradient axis between the application of the two gradient lobes. In a normal diffusion process, r is distributed according to a normal distribution $N(r,t)$, evaluated at $t = \tau_\Delta$. The complex-valued macroscopic MRI signal $S = S_0 e^{i\varphi}$ (see Eq. (15.5), Chap. 15) of a voxel can then be expressed by integration over all spins within that voxel:

$$S = S_0 \int_{-\infty}^{\infty} e^{i\varphi(r)} N(r, \tau_\Delta) \, dr = S_0 \int_{-\infty}^{\infty} e^{-i\gamma g \tau r} N(r,\tau) \, dr = S_0 e^{\overbrace{\frac{-\gamma^2 g^2 \tau^2 \tau_\Delta D}{b}}}. \quad (2.68)$$

All MRI-specific parameters, such as gyromagnetic ratio γ and gradient amplitude g, encoding time τ, or other timing variables, are usually collected in the "b-value." Note that the above formula for the b-value is only valid for short gradients with $\tau_\Delta \gg \tau$. Typically, diffusion-encoding gradients comprise positive and negative gradient lobes as well as a delay between the two, so that more complicated b-values result as exemplified in Fig. 2.6 and in Eq. (17.1) of Chap. 17. The monoexponential signal decay of Eq. (2.68) $S \sim e^{-bD}$ is considered as "regular diffusion" characterized by $\langle \mathbf{r}_2 \rangle \propto t$ [4]. In the presence of two compartments (e.g., intra-and extracellular water) with different diffusion coefficients, one would observe a bi-exponential decay. The bi-exponential model can be generalized to a multicompartment model, which predicts a stretched exponential decay of the form $S \sim e^{-b^\alpha D}$ with $\alpha < 1$ for a complex static environment in which diffusion is constrained [35]. In that case of "anomalous diffusion," the mean squared displacement is a power law in time, i.e., $\langle \mathbf{r}_2 \rangle \propto t^\alpha$. Note the similarity of this power law to the springpot given in Eq. (2.43), which is due to conceptual similarities between hierarchic structures in water diffusion and viscoelastic networks. Equation (2.68) can be further generalized by accounting for direction-dependent diffusion constants which evoke a 3×3 diffusion tensor $\mathbf{D}$, which is, similar to strain and stress, symmetric and has thus six independent entries. The eigenvalues of $\mathbf{D}$ represent three independent diffusion coefficients along the three Cartesian axes of the diffusion eigensystem
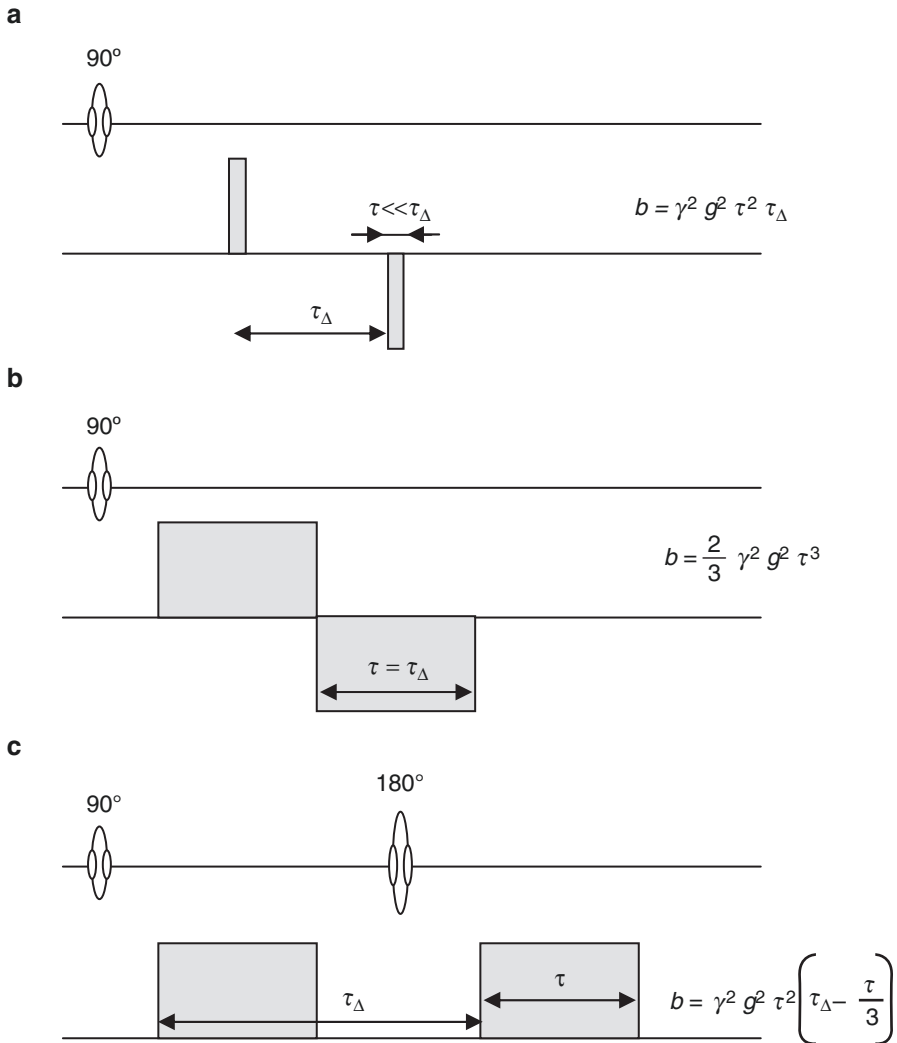
a

b

c

Fig. 2.6 Three basic diffusion-weighted MRI sequences and corresponding b-values. (**a**,**b**) Gradient echo sequence, (**c**) spin echo sequence; all with rectangular motion-encoding gradients (*gray rectangles*)

corresponding to the spread of particles in 3D and implying that diffusion is not a vector such as coherent flow. The MRI signal decay for anisotropic diffusion depends on the direction vectors **g** of the motion-encoding gradient: $S \sim e^{-b\mathbf{g}^T \cdot \mathbf{D} \cdot \mathbf{g}}$. Further details and applications of diffusion tensor imaging (DTI) are given in Chap. 17. It is worthwhile to mention that DTI normally accounts for restricted diffusion in the spatial-directional dimension. However, the restriction of water molecules moving against spatial boundaries is different at different propagation times t.

Table 2.2 Classification of diffusion as used in the literature of medical imaging

	Mean path lengths	MRI signal
Regular diffusion	$\langle \mathbf{r}^2 \rangle \propto D t$	$S \sim e^{-bD}$
Anomalous diffusion	$\langle \mathbf{r}^2 \rangle \propto D t^{\alpha}$	$S \sim e^{-b^{\alpha}D}$
Anisotropic diffusion	$\langle r_i r_j \rangle \propto D_{ij} t$	$S \sim e^{-b\mathbf{g}^T \cdot \mathbf{D} \cdot \mathbf{g}}$
Restricted diffusion (kurtosis imaging)	$\mathbf{r}^2 \propto D t \cdot \left(1 + \sqrt{K}\right)_a$	$S \sim e^{-bD + \frac{1}{6} b^2 D^2 K}$

[a]K is proportional to the excess kurtosis parameter used in the literature including all model-dependent prefactors [36]

The longer the molecules travel, the higher the probability for them to hit a restricting boundary in the tissue. For that reason, the diffusion profile is in general not characterized by a Gaussian distribution but by some deviating probability function. The excess diffusion kurtosis, also called "diffusion kurtosis," measures the deviation of the probability distribution function from a Gaussian curve and can be used to quantify heterogeneity of the diffusion environment [36]. Table 2.2 summarizes the discussed cases of the diffusion MRI signal.

2.7.4   Arterial Spin Labeling

Like diffusion MRI, perfusion MRI based on arterial spin labeling (ASL, also called arterial spin tagging, AST) is a difference technique, where the change in image intensity between a motion-sensitized scan and a non-sensitized reference scan is quantified and correlated with an underlying transport process. In ASL, contrast is generated by manipulating the magnetization of inflowing blood in such a way that it reduces the MR signal [37]. The spins in the inflowing blood are inverted by an 180° RF pulse prior to flowing into the volume of interest. Within that volume, they mix with the spins of the tissue. The inverted spins cause a reduction of the total magnetization since they cancel a part of the non-inverted tissue magnetization. As a consequence, the amplitude of the MR signal is reduced compared to the non-labeled reference image, leading to slight hypointensity in well-perfused regions. However, the contrast change is very subtle (on the order of 1–2%), requiring extensive signal averaging through repeated measurements. Furthermore, additional confounders have to be excluded as far as possible, leading to more refined and complex ASL MR sequences than explained above. In general, two types of ASL techniques exist: pulsed ASL (pASL), where a labeling pulse is deployed prior to every image acquisition, and continuous ASL (cASL), which aims to establish a steady state of labeled and unlabeled magnetization, necessitating a larger number of tagging pulses. A more in-depth discussion of different ASL techniques can be found in [33], among others.

2.8   Quantification of Other Structure-Related Parameters by Medical Imaging

Quantitative mapping of biophysical parameters other than those discussed above has a long tradition in medical imaging. One of the first quantitative and system-independent parameters measured by medical imaging was volume (volumetry). Tissue volume is often related to physiological functions of organs or the progression of diseases. For example, brain volume segmentation based on 3D MRI is the current gold standard for quantification of atrophy in neurodegenerative diseases [38]. Another example is muscle volume measurement by cardiac MRI or echocardiography as a direct measure of cardiac hypertrophy, which has wide implications for heart function [39]. Furthermore, the ejection fraction of the heart is a measure of systolic function [40]. The ejection fraction is calculated by dividing the stroke volume by the end-diastolic volume of the left ventricle. Slow changes in soft tissue volumes are regularly measured in longitudinal imaging examinations for quantifying tumor growth or the response to tumor treatment [41, 42].

Related to volume and mass is density, which, however, needs assumptions when estimated by medical imaging since tissue mass is normally not directly measurable. X-ray attenuation coefficients are highly dependent on tissue density and are thus exploited for quantifying bone density. Dual-energy X-ray absorptiometry (DXA) is the current gold standard for bone (mineral) density measurement as required for diagnosing and staging osteoporosis [43]. Quantification of minerals accumulated in soft tissues, such as calcifications in breast tumors, would be highly relevant for tumor staging [44, 45]. Morphology, location, and quantity of calcifications in the breast are established markers used in the BI-RADS atlas for breast tumor classification [46]. A further example is the quantification of iron in brain matter by MRI. Iron is the most abundant trace element in the human brain and plays an important role in maturation of the central nervous system and brain metabolism. Deposits of iron in the brain could cause neurological diseases like Alzheimer and Parkinson [47]. Susceptibility mapping by MRI can be used to quantify the spatial deposition of iron, e.g., in the human brain, but cannot quantify absolute iron content [48]. For the liver, iron content measurements based on relaxometry have been demonstrated [49]. Exogenous susceptibility sources such as gadolinium-based contrast agents induce magnetic susceptibility values which are theoretically linearly proportional to the concentration of the contrast agent. Thus, susceptibility mapping has the potential for in vivo quantification of contrast agent concentrations [50]. The ability of paramagnetic metal ions like iron or gadolinium to shorten magnetic relaxation is used in MRI contrast agents for the manipulation of image contrast in regions where water protons can interact with the contrast agent. Most clinically used MRI contrast agents reduce the T_1 relaxation time of protons by interaction with the nearby contrast agent. However, quantification of the amount of contrast agent in tissue by relaxation times is difficult since magnetic relaxation depends on the MRI system. Nevertheless, relaxation times constitute the primary contrast in MRI and are useful for the quantification of tissue properties as detailed for the myocardium in Chap. 15. Measurement of different water proton

relaxation mechanisms such as T_2 and effective T_2 (T_2*) allows estimation of vessel size and blood volume in the tissue [51, 52], which are both highly relevant biophysical parameters for characterizing tissue physiology and pathology [53]. Paired with perfusion measurements, vessel size and blood volume provide the input parameters for deriving hemodynamic constants such as hydraulic conductivity of the blood through the capillary bed of the tissue based on Darcy's law (see Chap. 3) [54]. Further structure-related biophysical and medical imaging-based parameters include geometry of vessels or fibers as can be quantified by bifurcation indices, tortuosity, self-similarity, structural density, and fractal dimension [55].

Conclusion

State-of-the-art medical imaging offers a wide range of sensitivities to motion in the human body. From incoherent motion of water molecules to coherent flow, medical imaging modalities can be used to depict physiologic and dysfunctional transport phenomena and to derive quantitative imaging markers for clinical diagnosis. This chapter summarized the physics of transport from an imaging point of view and reviewed the basic concepts of motion encoding in medical imaging. It was shown that very basic assumptions such as continuity of mass and energy at the position of the measurement can lead to a rich set of equations that explain multiple phenomena observed by motion-sensitive imaging modalities including diffusion, perfusion, and flow imaging as well as elastography. Since transport-related parameters and mechanical constants are of huge importance for the quantification of constitution and function of biological tissues, this chapter presents a primer of quantitative biophysical medical imaging.

References

1. Feynman RP, Leighton RB, Sands M, Feynman P. The Feynman lectures on physics, volume II: the new millennium edition: mainly electromagnetism and matter. New York: Basic Books; 2015.
2. Feynman RP, Leighton RB, Sands M, Feynman P. The Feynman lectures on physics, volume I: the new millennium edition: mainly mechanics, radiation, and heat. New York: Basic Books; 2015.
3. Einstein A. Über die von der molekularkinetischen Theorie der Wärme geforderte Bewegung von in ruhenden Flüssigkeiten suspendierten Teilchen. Ann Phys. 1905;17(8):549–60.
4. Ben-Avraham D, Havlin S. Diffusion and reactions and disordered systems. Cambridge: Cambridge University Press; 2000.
5. Landau LD, Lifschitz EM. Theory of elasticity. Oxford: Pergamon; 1986.
6. Lai WM, Rubin D, Krempl E. Introduction to continuum mechanics. Burlington: Butterworth Heinemann; 1994. 570 p.
7. Fedorov FI. Theory of elastic waves in crystals. New York: Plenum; 1968.
8. Parker KJ, Huang SR, Musulin RA, Lerner RM. Tissue response to mechanical vibrations for "sonoelasticity imaging". Ultrasound Med Biol. 1990;16(3):241–6.
9. Muthupillai R, Ehman RL. Magnetic resonance elastography. Nat Med. 1996;2(5):601–3.
10. Manduca A, Oliphant TE, Dresner MA, Mahowald JL, Kruse SA, Amromin E, Felmlee JP, Greenleaf JF, Ehman RL. Magnetic resonance elastography: non-invasive mapping of tissue elasticity. Med Image Anal. 2001;5(4):237–54.

11. Hirsch S, Braun J, Sack I. Magnetic resonance elastography: physical background and medical applications. Weinheim: Wiley; 2017.

12. Romano AJ, Shirron JJ, Bucaro JA. On the noninvasive determination of material parameters from a knowledge of elastic displacements theory and numerical simulation. IEEE Trans Ultrason Ferroelectr Freq Control. 1998;45(3):751–9.

13. Romano AJ, Bucaro JA, Ehnan RL, Shirron JJ. Evaluation of a material parameter extraction algorithm using MRI-based displacement measurements. IEEE Trans Ultrason Ferroelectr Freq Control. 2000;47(6):1575–81.

14. Park E, Maniatty AM. Shear modulus reconstruction in dynamic elastography: time harmonic case. Phys Med Biol. 2006;51(15):3697–721.

15. Oliphant TE, Manduca A, Ehman RL, Greenleaf JF. Complex-valued stiffness reconstruction for magnetic resonance elastography by algebraic inversion of the differential equation. Magn Reson Med. 2001;45:299–310.

16. Hirsch S, Klatt D, Freimann F, Scheel M, Braun J, Sack I. In vivo measurement of volumetric strain in the human brain induced by arterial pulsation and harmonic waves. Magn Reson Med. 2012;70(3):671–83.

17. Mousavi SR, Fehlner A, Streitberger KJ, Braun J, Samani A, Sack I. Measurement of in vivo cerebral volumetric strain induced by the Valsalva maneuver. J Biomech. 2014;47(7):1652–7.

18. Aki K, Richards PG. Quantitative seismology. Sausalito: Universtiy Science Books; 2002.

19. Fink M, Montaldo G, Tanter M. Time-reversal acoustics in biomedical engineering. Annu Rev Biomed Eng. 2003;5:465–97.

20. Mainardi F. Fractional calculus and waves in linear viscoelasticity. London: Imperial College Press; 2010.

21. Magin RL. Fractional calculus in bioengineering. Crit Rev Biomed Eng. 2004;32(1):1–104.

22. Fabry B, Maksym GN, Butler JP, Glogauer M, Navajas D, Taback NA, Millet EJ, Fredberg JJ. Time scale and other invariants of integrative mechanical behavior in living cells. Phys Rev E Stat Nonlinear Soft Matter Phys. 2003;68(4 Pt 1):041914.

23. Sack I, Joehrens K, Wuerfel E, Braun J. Structure sensitive elastography: on the viscoelastic powerlaw behavior of in vivo human tissue in health and disease. Soft Matter. 2013;9(24):5672–80.

24. Tschoegl NW. The phenomenological theory of linear viscoelastic behavior. Berlin: Springer; 1989.

25. Achenbach JD. Wave propagation in elastic solids. Amsterdam: Elsevier; 1999.

26. Fenster A, Lacefield JC. In: Karellas A, editor. Ultrasound imaging and therapy. Boca Raton: CRC Press; 2015.

27. Stankovic Z, Allen BD, Garcia J, Jarvis KB, Markl M. 4D flow imaging with MRI. Cardiovasc Diagn Ther. 2014;4(2):173–92.

28. Thomas DL, Lythgoe MF, Pell GS, Calamante F, Ordidge RJ. The measurement of diffusion and perfusion in biological systems using magnetic resonance imaging. Phys Med Biol. 2000;45(8):R97–138.

29. Le Bihan D. Theoretical principles of perfusion imaging. Application to magnetic resonance imaging. Investig Radiol. 1992;27(Suppl 2):S6–11.

30. Buxton RB. Quantifying CBF with arterial spin labeling. J Magn Reson Imaging. 2005;22(6):723–6.

31. Pesavento A, Perrey C, Krueger M, Ermert A. A Time-efficient and accurate strain estimation concept for ultrasonic elastography using iterative phase zero estimation. IEEE Trans Ultrason Ferroelectr Freq Control. 1999;46(5):1057–67.

32. Bamber J, Cosgrove D, Dietrich CF, Fromageau J, Bojunga J, Calliada F, Cantisani V, Correas JM, D'Onofrio M, Drakonaki EE, Fink M, Friedrich-Rust M, Gilja OH, Havre RF, Jenssen C, Klauser AS, Ohlinger R, Saftoiu A, Schaefer F, Sporea I, Piscaglia F. EFSUMB guidelines and recommendations on the clinical use of ultrasound elastography. Part 1: basic principles and technology. Ultraschall Med. 2013;34(2):169–84.

33. Bernstein MA, King KF, Zhou XJ. Handbook of MRI pulse sequences. Burlington: Elsevier Academic; 2004.

34. Stejskal EO, Tanner JE. Spin diffusion measurements: spin echoes in the presence of a time-dependent field gradient. J Chem Phys. 1965;42(1):288–92.
35. Hall MG, Barrick TR. From diffusion-weighted MRI to anomalous diffusion imaging. Magn Reson Med. 2008;59(3):447–55.
36. Jensen JH, Helpern JA. MRI quantification of non-Gaussian water diffusion by kurtosis analysis. NMR Biomed. 2010;23(7):698–710.
37. Detre JA, Leigh JS, Williams DS, Koretsky AP. Perfusion imaging. Magn Reson Med. 1992;23(1):37–45.
38. Despotovic I, Goossens B, Philips W. MRI segmentation of the human brain: challenges, methods, and applications. Comput Math Methods Med. 2015;2015:450341.
39. Maceira AM, Mohiaddin RH. Cardiovascular magnetic resonance in systemic hypertension. J Cardiovasc Magn Reson. 2012;14:28.
40. Lang RM, Bierig M, Devereux RB, Flachskampf FA, Foster E, Pellikka PA, Picard MH, Roman MJ, Seward J, Shanewise JS, Solomon SD, Spencer KT, Sutton MS, Stewart WJ. Recommendations for chamber quantification: a report from the American Society of Echocardiography's Guidelines and Standards Committee and the Chamber Quantification Writing Group, developed in conjunction with the European Association of Echocardiography, a branch of the European Society of Cardiology. J Am Soc Echocardiogr. 2005;18(12):1440–63.
41. Andreopoulou E, Andreopoulos D, Adamidis K, Fountzila-Kalogera A, Fountzilas G, Dimopoulos MA, Aravantinos G, Zamboglou N, Baltas D, Pavlidis N. Tumor volumetry as predictive and prognostic factor in the management of ovarian cancer. Anticancer Res. 2002;22(3):1903–8.
42. Iliadis G, Kotoula V, Chatzisotiriou A, Televantou D, Eleftheraki AG, Lambaki S, Misailidou D, Selviaridis P, Fountzilas G. Volumetric and MGMT parameters in glioblastoma patients: survival analysis. BMC Cancer. 2012;12:3.
43. Blake GM, Fogelman I. Technical principles of dual energy x-ray absorptiometry. Semin Nucl Med. 1997;27(3):210–28.
44. Grigoryev M, Thomas A, Plath L, Durmus T, Slowinski T, Diekmann F, Fischer T. Detection of microcalcifications in women with dense breasts and hypoechoic focal lesions: comparison of mammography and ultrasound. Ultraschall Med. 2014;35(6):554–60.
45. Naseem M, Murray J, Hilton JF, Karamchandani J, Muradali D, Faragalla H, Polenz C, Han D, Bell DC, Brezden-Masley C. Mammographic microcalcifications and breast cancer tumorigenesis: a radiologic-pathologic analysis. BMC Cancer. 2015;15:307.
46. Bassett LW. Standardized reporting for mammography: BI-RADS. Breast J. 1997;3:207–10.
47. Ward RJ, Zucca FA, Duyn JH, Crichton RR, Zecca L. The role of iron in brain ageing and neurodegenerative disorders. Lancet. 2014;13(10):1045–60.
48. Deistung A, Schweser F, Reichenbach JR. Overview of quantitative susceptibility mapping. NMR Biomed. 2016;30:e3569.
49. Kannengiesser S. Iron quantification with LiverLab. MAGNETOM Flash. 2016;3(66):44–6.
50. de Rochefort L, Nguyen T, Brown R, Spincemaille P, Choi G, Weinsaft J, Prince MR, Wang Y. In vivo quantification of contrast agent concentration using the induced magnetic field for time-resolved arterial input function measurement with MRI. Med Phys. 2008;35(12):5328–39.
51. Tropres I, Grimault S, Vaeth A, Grillon E, Julien C, Payen JF, Lamalle L, Decorps M. Vessel size imaging. Magn Reson Med. 2001;45(3):397–408.
52. Shen Y, Pu IM, Ahearn T, Clemence M, Schwarzbauer C. Quantification of venous vessel size in human brain in response to hypercapnia and hyperoxia using magnetic resonance imaging. Magn Reson Med. 2013;69(6):1541–52.
53. Emblem KE, Mouridsen K, Bjornerud A, Farrar CT, Jennings D, Borra RJ, Wen PY, Ivy P, Batchelor TT, Rosen BR, Jain RK, Sorensen AG. Vessel architectural imaging identifies cancer patient responders to anti-angiogenic therapy. Nat Med. 2013;19(9):1178–83.
54. Hetzer S, Birr P, Fehlner A, Hirsch S, Dittmann F, Barnhill E, Braun J, Sack I. Perfusion alters stiffness of deep gray matter. J Cereb Blood Flow Metab. 2017:271678X17691530.
55. Bankman I. In: Bankman I, editor. Handbook of medical image processing and analysis. Amsterdam: Elsevier; 2009.